

# 福昕PDF编辑器

• 永久 • 轻巧 • 自由

升级会员

批量购买



永久使用

无限制使用次数



极速轻巧

超低资源占用，告别卡顿慢



自由编辑

享受Word一样的编辑自由



手机 扫一扫，关注公众号



## Regular article

# Small infrared target detection using absolute average difference weighted by cumulative directional derivatives

Saeid Aghaziyarati<sup>a</sup>, Saed Moradi<sup>b,\*</sup>, Hasan Talebi<sup>c</sup><sup>a</sup> Faculty of Engineering, Shahid Bahonar University of Kerman, Kerman, Iran<sup>b</sup> Department of Electrical Engineering, Faculty of Engineering, University of Isfahan, Isfahan, Iran<sup>c</sup> Department of Mechatronics Engineering, Science and Research Branch, Islamic Azad University, Tehran, Iran

## ARTICLE INFO

## Keywords:

Small infrared target detection  
Average absolute gray difference  
Structural background removal  
Cumulative directional derivatives

## ABSTRACT

Infrared search and track (IRST) systems have attracted more attention in recent years due to advances of infrared imaging technology. In a typical IRST system, small infrared detection algorithm is the most challenging part of the system development procedure. In this paper, an effective algorithm based on the average absolute gray difference (AAGD) is presented. In the first step, the main deficiencies of the AAGD algorithm are investigated precisely. After identifying three major drawbacks of the AAGD algorithm, a powerful small target detection algorithm is developed through compensating every single weak-spot in the AAGD algorithm. The simulation results on real infrared images prove that the proposed algorithm not only compensates the AAGD disadvantages but also outperforms the recently published well-known small infrared target detection algorithms in both qualitative and quantitative perspectives.

## 1. Introduction

Infrared search and track (IRST) systems have attracted researchers' attention during the past decade due to their specifications like covert operation and robustness against jamming and electronic interference [1–4]. However, detecting long-distant small targets in infrared images is a challenging task because of low signal to noise ratio (SNR) and complicated background clutter [5–7].

There are too many researches which are dedicated to small infrared target detection field in the literature. Generally, these researches can be categorized into two main groups [8]. The first group includes methods which are based on background subtraction. In this approach, in the first step, the background is approximated using desired operators like max-median [9], max-mean [9], morphology opening [10], and principal component pursuit (PCP) [11]. Then, the approximated background is subtracted from the original image. Finally, the targets are extracted using a proper thresholding strategy [12]. While this approach is straightforward and has low computational complexity, it suffers from high false alarm rate where the true background is not accurately approximated [13].

The second approach in small infrared target detection field directly enhances target region and suppresses the background area [8]. Considering the Gaussian model for the spatial distribution of the small targets, normalized Laplacian of Gaussian (LoG) is adopted in a scale-

space manner to resolve target size variation during successive infrared frames [14]. While this method is able to intensify low signal to clutter ratio (low SCR) targets, it is sensitive to background noise due to utilizing second order derivatives. Local contrast method (LCM) target detection [15] and its improved versions [16,17] show good target enhancement ability. However, considering the maximum intensity of the area under test as a figure of merit makes these algorithms sensitive to salt noise (single pixel noise with maximum intensity). Also, using a local background window to implement these algorithms attenuates targets which are maneuvering close to a high-intensity background clutter. The average absolute gray difference (AAGD) [18] is a relatively powerful and robust infrared small target detection algorithm. While the AAGD can effectively suppress background noise (thanks to local averaging feature) and enhance weak small targets, this algorithm is sensitive to high-intensity edges. Moreover, this algorithm utilizes local background window just like the other local contrast based algorithms, which in turns, increases target miss rate when the target is close to high-intensity edge. Patch based contrast measure (PCM) [19] is an improved version of LCM which considers local averaging instead of maximum selection for the area under the test. Since this algorithm utilizes background patches, it suffers from the challenge which arises when the target maneuvering close to a high-intensity clutter. Also, negative values in the filtered image after performing PCM algorithm shifts zero values to higher level after normalizing the filtered image,

\* Corresponding author.

E-mail address: [s.moradi@eng.ui.ac.ir](mailto:s.moradi@eng.ui.ac.ir) (S. Moradi).

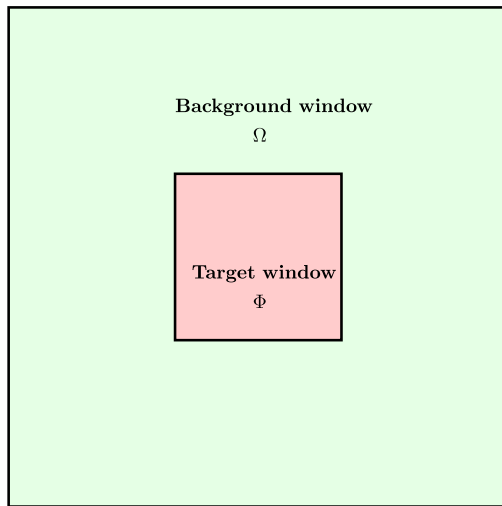


**Fig. 1.** Target and background windows in AAGD algorithm.

which in turns, increases false responses.

According to the aforementioned information, intensifying high-intensity structural backgrounds and missing targets which are maneuvering close to a high-intensity background clutter are two unsolved challenges in small infrared target detection field. In this paper, an effective method is proposed to eliminate these drawbacks and develop robust small infrared target detection algorithm. The rest of this paper is organized as follows: the next section is devoted to the background and motivation of this work. The proposed method is presented in section three. Simulation results are provided in section four to demonstrate the effectiveness of the proposed algorithm. Finally, the paper is concluded in section five.

## 2. Background and motivation

One of the most efficacious small target detection algorithm which directly benefits from local contrast of the target area is the average absolute gray difference (AAGD). The detection mechanism of this algorithm is based on natural contrast between the infrared target area and its surrounding local background. Considering two local nested windows for each pixel (Fig. 1), in this algorithm, the absolute difference between the average value of the pixels which belong to the target window ( $\Phi$ ) and the average value of the pixels which belong to the

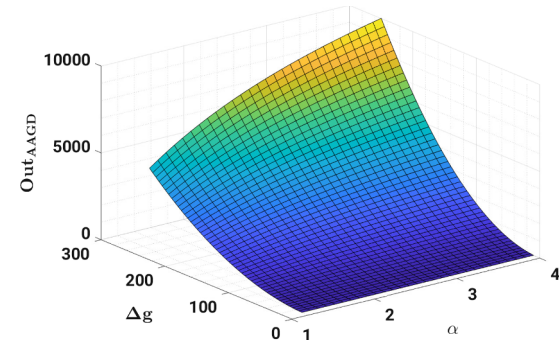


**Fig. 3.** The output response of the AAGD algorithm to a step edge.

background window ( $\Omega$ ) is computed as the output value. Thus, the output value of each pixel after performing the AAGD algorithm on the original infrared image can be expressed as [18]:

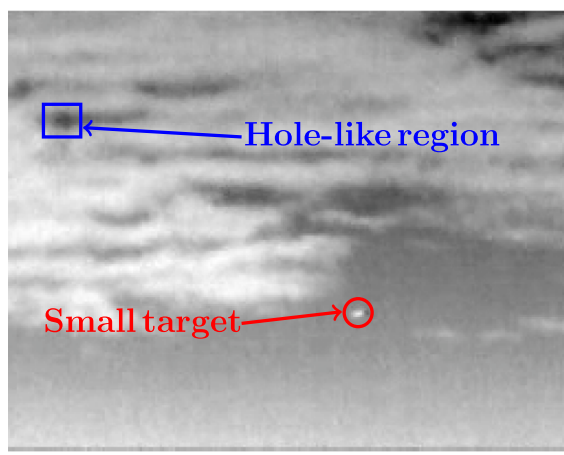
$$AAGD = |\mu_\Phi - \mu_\Omega|^2 = \left| \frac{1}{N_\Phi} \sum_{(s,t) \in \Phi} I(s, t) - \frac{1}{N_\Omega} \sum_{(p,q) \in \Omega} I(p, q) \right|^2, \quad (1)$$

where  $I(x, y)$ ,  $N_\Phi$  and  $N_\Omega$  stand for the pixel intensity at position  $(x, y)$ , the total number of pixels contained in the set  $\Phi$  and the total number of pixels contained in the set  $\Omega$ , respectively.

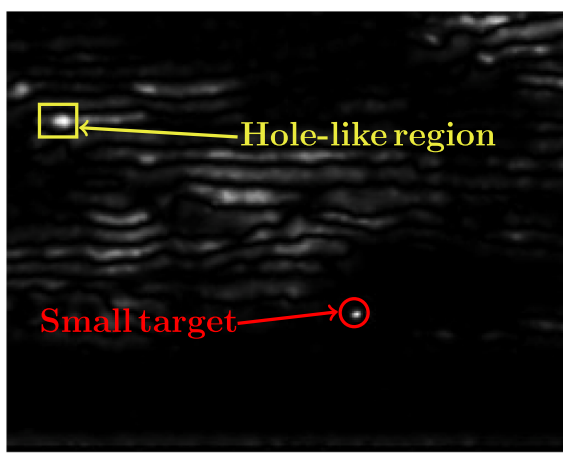
Since AAGD benefits from the local averaging operator, it can effectively suppress background noise. Also, since this algorithm can be implemented using local averaging, real-time operation is easily achieved. While the AAGD algorithm has outstanding performance in practical as well as noisy scenarios, this algorithm suffers from three main limitations which are comprehensively described as follows.

First, since there is no distinction between positive and negative contrasts in AAGD formulation (Eq. (1)), the regions with both positive local contrast (target area) and negative local contrast (hole-like regions) will be intensified (Fig. 2). As shown in Fig. 2, the corresponding regions to hole-like regions (blue rectangle) are enhanced wrongly, which in turns, increases false alarm rate.

Second, when the background of infrared images contains high-intensity sharp edges, the detection performance of the AAGD algorithm decreases dramatically. For the sake of better understanding of this challenge, a simple yet convincing scenario is presented in Fig. 4. Without loss of generality, let assume that the step edge in background area (Fig. 4b) just has two gray levels ( $g_b$  and  $g_d$  values for bright and dark areas, respectively), and the AAGD algorithm is just constructed in



(a)



(b)

**Fig. 2.** The first limitation of AAGD algorithm. (a) Original image, (b) the AAGD response to (a).

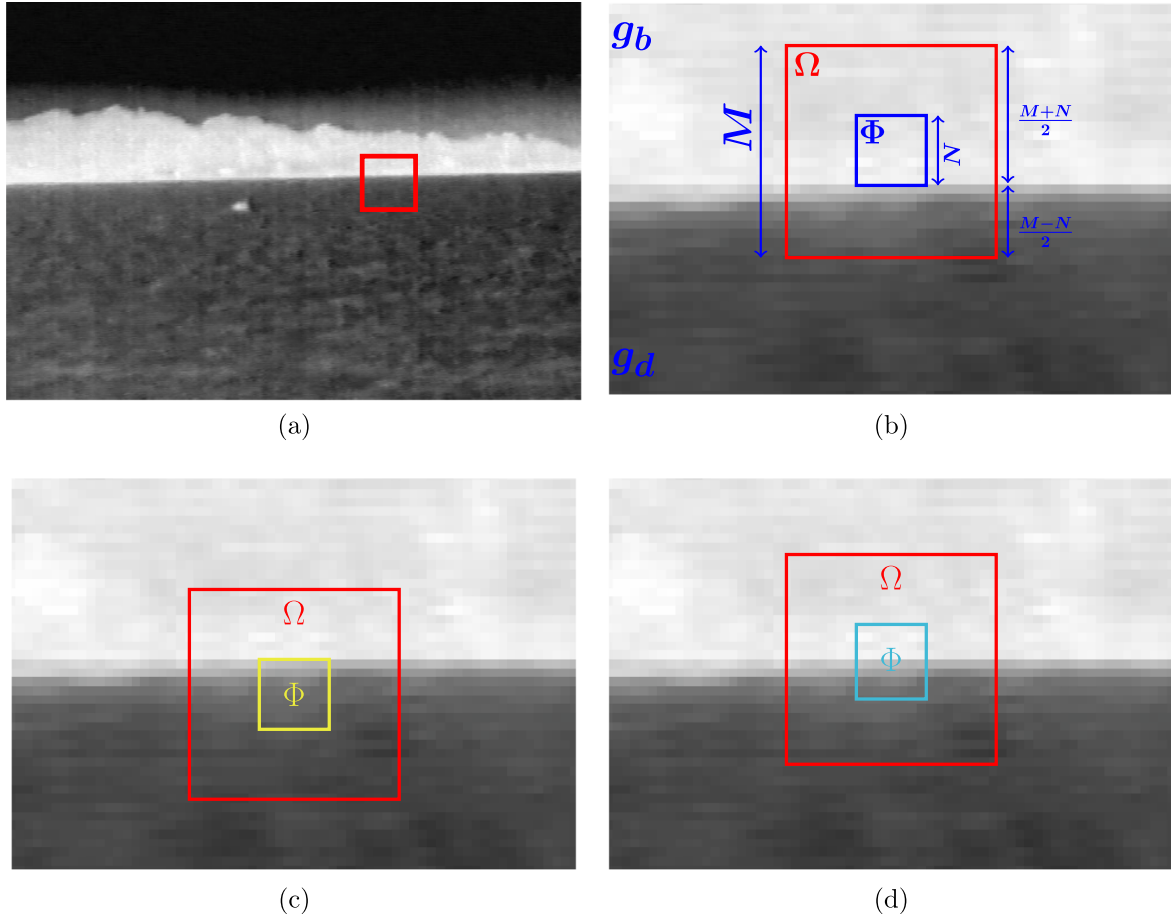


**Fig. 4.** A simple scenario to demonstrate the second limitation of AAGD algorithm. (a) Original infrared image containing sharp edges, (b) the target window has positive contrast compare to the local background, (c) the target window has negative contrast compare to the local background, (d) the center of the target window is exactly lies on the edge.

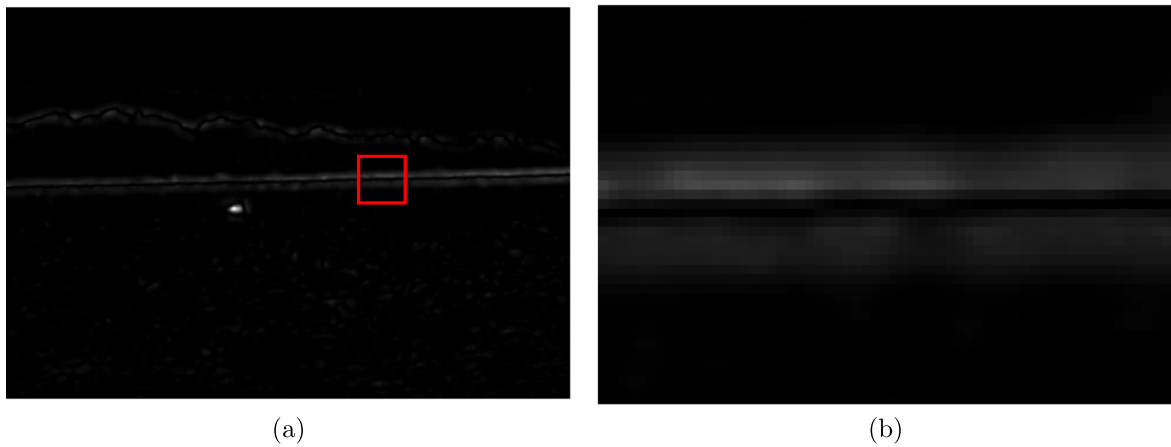


**Fig. 5.** AAGD response to a real infrared scenario containing sharp edges, (a) AAGD response to Fig. 4a, (b) zoomed area of the red rectangle in (a). (For interpretation of the references to color in this figure legend, the reader is referred to the web version of this article.)

a single scale. Also, let assume that the sizes of external window and internal window are set to be  $M \times M$  and  $N \times N$  pixels, respectively. In the first scenario (Fig. 4b), the target window completely lies in the bright area. In this situation, the average intensity of the internal window ( $\mu_\Phi$ ) is equal to  $g_b$ , obviously. The average intensity of the  $\Omega$  set ( $\mu_\Omega$ ) can be calculated as:

$$\begin{aligned} \mu_\Omega &= \frac{\left(M \times \left(\frac{M+N}{2}\right) - N^2\right) \times g_b + \left(M \times \left(\frac{M-N}{2}\right)\right) \times g_d}{M^2 - N^2} \\ &= \frac{\left(\frac{M^2 + M \times N - 2N^2}{2}\right) \times g_b + \left(\frac{M^2 - M \times N}{2}\right) \times g_d}{M^2 - N^2} \\ &= \frac{(M^2 + M \times N - 2N^2) \times g_b + (M^2 - M \times N) \times g_d}{2(M^2 - N^2)} \end{aligned} \quad (2)$$

Hence, the output of the AAGD algorithm can be calculated as:

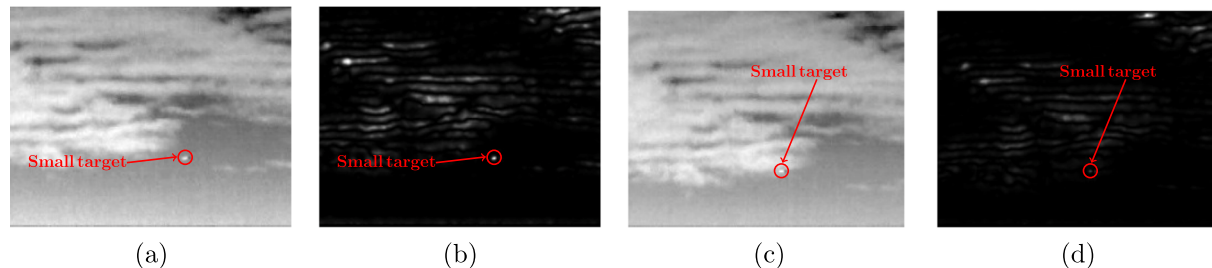


**Fig. 6.** A simple scenario to demonstrate the third limitation of AAGD algorithm. (a) Original infrared image containing a target far from a high-intensity cloud edge, (b) AAGD response to (a), (c) original infrared image containing a target close to a high-intensity cloud edge, (d) AAGD response to (c).

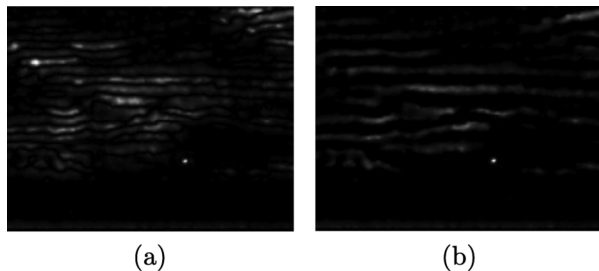


**Fig. 7.** Eliminating the hole-like objects (negative contrasts), (a) the AAGD response to Fig. 2a, (b) eliminating the hole-like objects based on Eq. (8).

$$\begin{aligned} out_{AAGD} &= (\mu_\Phi - \mu_\Omega)^2 \\ &= \left( g_b - \frac{(M^2 + M \times N - 2N^2) \times g_b + (M^2 - M \times N) \times g_d}{2(M^2 - N^2)} \right)^2 \\ &= \left( \left( \frac{M^2 - M \times N}{2(M^2 - N^2)} \right) \times (g_b - g_d) \right)^2 \\ &= \left( \left( \frac{M^2 - M \times N}{2(M^2 - N^2)} \right) \times \Delta g \right)^2 \end{aligned} \quad (3)$$

where,  $\Delta g$  demonstrates the sharpness of the edge.

Since the external window is always bigger than internal window, let assume  $M = \alpha N$  where,  $\alpha > 1$ . Therefore, Eq. (3) can be rewritten as:

$$\begin{aligned} out_{AAGD} &= \left( \left( \frac{(\alpha N)^2 - (\alpha N) \times N}{2((\alpha N)^2 - N^2)} \right) \times \Delta g \right)^2 \\ &= \left( \left( \frac{\alpha^2 N^2 - \alpha N^2}{2((\alpha^2 - 1)N^2)} \right) \times \Delta g \right)^2 \\ &= \left( \left( \frac{\alpha^2 - \alpha}{2(\alpha^2 - 1)} \right) \times \Delta g \right)^2 \\ &= \left( \frac{\alpha}{2(\alpha + 1)} \right)^2 \times \Delta g^2 \end{aligned} \quad (4)$$

According to Eq. (4), as  $\Delta g$  increases (the edge becomes more sharper), the response of the AAGD algorithm to the edge becomes more intensified (Fig. 3).

When the internal window has a negative contrast compared to the external background (Fig. 4c), the average intensity of the internal window ( $\mu_\Phi$ ) is equal to  $g_d$ . The average intensity of the  $\Omega$  set ( $\mu_\Omega$ ) can

be calculated as:

$$\begin{aligned} \mu_\Omega &= \frac{\left( M \times \left( \frac{M+N}{2} \right) - N^2 \right) \times g_d + \left( M \times \left( \frac{M-N}{2} \right) \right) \times g_b}{M^2 - N^2} \\ &= \frac{\left( \frac{M^2 + M \times N - 2N^2}{2} \right) \times g_d + \left( \frac{M^2 - M \times N}{2} \right) \times g_b}{M^2 - N^2} \\ &= \frac{(M^2 + M \times N - 2N^2) \times g_d + (M^2 - M \times N) \times g_b}{2(M^2 - N^2)} \end{aligned} \quad (5)$$

Hence, the output of the AAGD algorithm can be calculated as:

$$\begin{aligned} out_{AAGD} &= (\mu_\Phi - \mu_\Omega)^2 \\ &= \left( g_d - \frac{(M^2 + M \times N - 2N^2) \times g_d + (M^2 - M \times N) \times g_b}{2(M^2 - N^2)} \right)^2 \\ &= \left( \left( \frac{M^2 - M \times N}{2(M^2 - N^2)} \right) \times (g_d - g_b) \right)^2 \\ &= \left( \left( \frac{M^2 - M \times N}{2(M^2 - N^2)} \right) \times (-\Delta g) \right)^2 \end{aligned} \quad (6)$$

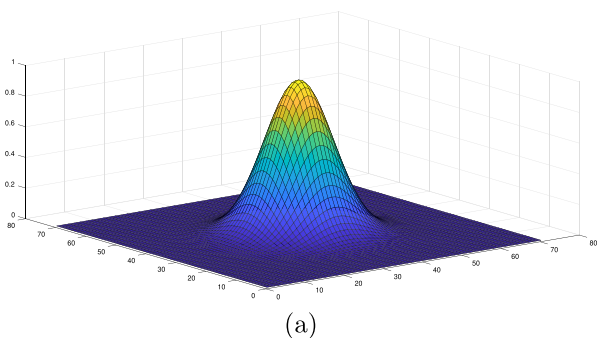
By substituting  $M = \alpha N$  in Eq. (6) and making some simplifications, we have:

$$\begin{aligned} out_{AAGD} &= \left( \left( \frac{\alpha^2 - \alpha}{2(\alpha^2 - 1)} \right) \times (-\Delta g) \right)^2 \\ &= \left( \frac{\alpha}{2(\alpha + 1)} \right)^2 \times \Delta g^2 \end{aligned} \quad (7)$$

Eq. (7) demonstrates that similar to the former scenario (Fig. 4b), the AAGD algorithm returns a strong response to the non-target area. The response is directly proportional to square of the edge sharpness ( $\Delta g$ ). While the response to an sharp edge can be degraded by choosing appropriate window size (i.e. the  $\alpha$  parameter), it cannot be completely eliminated using AAGD algorithm (Fig. 3).

When the center of the target window exactly lies on the edge (Fig. 4d), the AAGD output takes zero value. This is why there is a dark area between two parallel lines in the AAGD output (Fig. 5b).

As the last drawback of the AAGD algorithm, this algorithm is unable to enhance targets maneuvering close to a high-intensity structural background. When the flying small target is close to a high-intensity structure like cloud edge, a large portion of background window ( $\Omega$ ) is occupied by the high-intensity background clutter which, in turn,



$G_N$						
$G_W$	$T_{W_2}$	$T_{W_1}$	$T_C$	$T_{E_1}$	$T_{E_2}$	$G_E$
			$T_{N_2}$			
			$T_{N_1}$			
				$T_{S_1}$		
				$T_{S_2}$		
				$G_S$		

(b)

**Fig. 8.** (a) Two dimensional Gaussian spatial distribution, (b)  $5 \times 5$  target window surrounded by a single pixel guard.

0 0 0 -1 0 0 0 0	0 0 0 -1 0 0 0 0	0 0 0 -1 0 0 0 0	0 0 0 -3 0 0 0 0
0 0 0 0 0 0 0 0	0 0 0 0 0 0 0 0	0 0 0 1 0 0 0 0	0 0 0 1 0 0 0 0
0 0 0 0 0 0 0 0	0 0 0 1 0 0 0 0	0 0 0 0 0 0 0 0	0 0 0 1 0 0 0 0
0 0 0 1 0 0 0 0	0 0 0 0 0 0 0 0	0 0 0 0 0 0 0 0	-3 1 1 4 1 1 -3
0 0 0 0 0 0 0 0	0 0 0 0 0 0 0 0	0 0 0 0 0 0 0 0	0 0 0 1 0 0 0 0
0 0 0 0 0 0 0 0	0 0 0 0 0 0 0 0	0 0 0 0 0 0 0 0	0 0 0 1 0 0 0 0
0 0 0 0 0 0 0 0	0 0 0 0 0 0 0 0	0 0 0 0 0 0 0 0	0 0 0 -3 0 0 0 0
0 0 0 0 0 0 0 0	0 0 0 0 0 0 0 0	0 0 0 0 0 0 0 0	0 0 0 0 0 0 0 0

(a)

(b)

(c)

(d)

**Fig. 9.** The proposed convolution kernels. (a) The convolution kernel corresponding Eq. (10a), (b) the convolution kernel corresponding Eq. (10b), (c) the convolution kernel corresponding Eq. (10c), (d) final two dimensional convolution kernel.

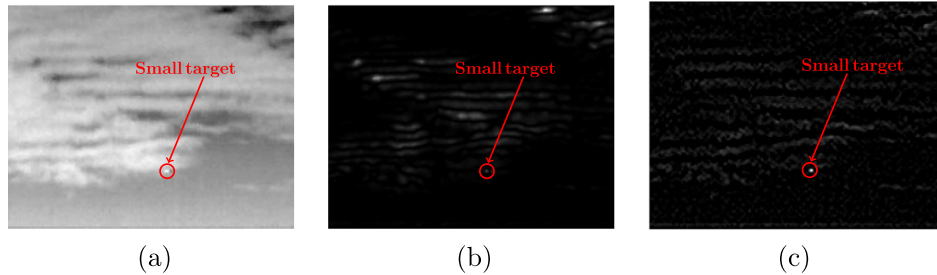


**Fig. 10.** (a) Original infrared image containing a target close to a high-intensity cloud edge, (b) AAGD response to (a), (c) the result of applying Fig. 9d kernel to (a).

0 0 0 -3 0 0 0 0	0 0 0 0 0 0 0 0	0 0 0 0 0 0 0 0	0 0 0 0 0 0 0 0
0 0 0 1 0 0 0 0	0 0 0 0 0 0 0 0	0 0 0 0 0 0 0 0	0 0 0 0 0 0 0 0
0 0 0 1 0 0 0 0	0 0 0 0 0 0 0 0	0 0 0 0 0 0 0 0	0 0 0 0 0 0 0 0
0 0 0 1 0 0 0 0	0 0 0 0 0 0 0 0	0 0 0 1 1 1 -3	0 0 0 0 0 0 0 0
0 0 0 0 0 0 0 0	0 0 0 0 0 0 0 0	0 0 0 0 0 0 0 0	0 0 0 0 0 0 0 0
0 0 0 0 0 0 0 0	0 0 0 0 0 0 0 0	0 0 0 0 1 0 0 0	0 0 0 0 0 0 0 0
0 0 0 0 0 0 0 0	0 0 0 0 0 0 0 0	0 0 0 0 1 0 0 0	0 0 0 0 0 0 0 0
0 0 0 0 0 0 0 0	0 0 0 0 0 0 0 0	0 0 0 0 1 0 0 0	0 0 0 0 0 0 0 0
0 0 0 0 0 0 0 0	0 0 0 0 0 0 0 0	0 0 0 0 1 0 0 0	0 0 0 0 0 0 0 0

(a)

(b)

(c)

(d)

**Fig. 11.** The proposed cumulative directional convolution kernels: (a)  $k_n$ , (b)  $k_e$ , (c)  $k_s$ , (d)  $k_w$ .

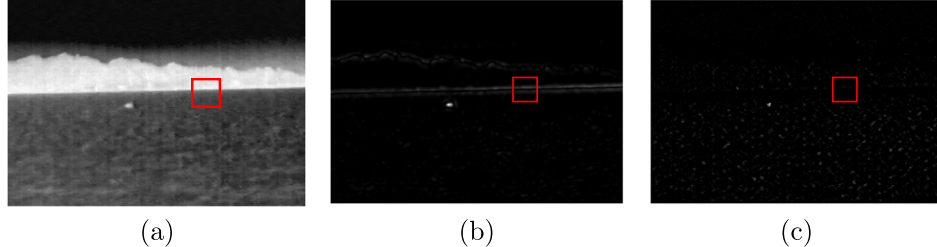


**Fig. 12.** (a) Original infrared image containing sharp edges, (b) AAGD response to (a), (c) the result of applying cumulative directional derivative kernels on (a) (the proposed weighting coefficients).

increases the average value of background window ( $\mu_\Omega$ ). Consequently, the AAGD target enhancement ability declines drastically. As shown in Fig. 6a, when the target lies on a homogeneous local background, the AAGD algorithm can effectively enhance target region (Fig. 6b). As the flying small target gets closer to the high-intensity cloud edge (Fig. 6c), the AAGD response to target area becomes more attenuated (Fig. 6d).

In this paper, the aforementioned three drawbacks of the AAGD algorithm are eliminated and powerful small target detection algorithm is constructed.

### 3. The proposed method

In this section, the aforementioned three drawbacks of the AAGD algorithm is eliminated step by step to construct robust and powerful small infrared target detection algorithm.

In the first step, the problem related to the hole-like object intensification is investigated. As shown in Fig. 2b, the AAGD algorithm treats the hole-like object like the true targets. This happens because of the AAGD filtering formulation (Eq. (1)). Since in Eq. (1) the absolute value of the difference between target and background window average

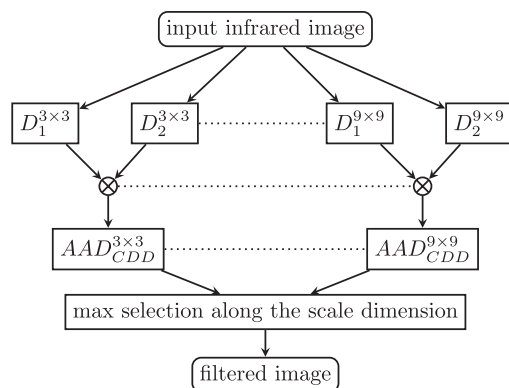


**Fig. 13.** The block diagram of the multi-scale implementation of the proposed algorithm.

values is considered as the output value, both negative and positive contrasts are enhanced, while the small infrared objects only have positive local contrast due to their higher temperature compared to surrounding environment. This problem can be easily addressed using new formulation for AAGD algorithm which is called improved AAGD:

$$D_1 = |\mu_\Phi - \mu_\Omega|^2 \times H(\mu_\Phi - \mu_\Omega) \quad (8)$$

where  $H(\cdot)$  is the Heaviside step function and expressed as:

$$H(x) = \begin{cases} 1 & x \geq 0 \\ 0 & x < 0 \end{cases} \quad (9)$$

**Fig. 7** demonstrates the hole-like objects elimination based on Eq. (8). As depicted in the figure, the traditional AAGD has many false responses in the filtered image (**Fig. 7a**). As shown in **Fig. 7b** these false responses are eliminated via thresholding process which is expressed in Eq. (8).

The problem related to the maneuvering targets close to a high-intensity structural background is not only limited to the AAGD algorithm. In fact, all the detection algorithms which utilize background window (e.g. PCM and LCM) suffer from this drawback. In order to eliminate this limitation and enhance the detection ability of the proposed algorithm, the spatial distribution of the target pixels is taken into account to construct effective convolution kernel for discrimination between the target and non-target areas.

The two-dimensional Gaussian distribution (**Fig. 8a**) is the most common model for modeling of the spatial distribution of the small infrared target [14]. While this modeling is a relatively rough approximation [20,8], it is a satisfactory model for our purpose. Let assume that the target area is completely fit into the target window (the blue rectangle in **Fig. 8b**) and the target window is surrounded by a single pixel guard (the area between the red and the blue rectangles in **Fig. 8b**). By considering two-dimensional Gaussian distribution for modeling of the spatial distribution of the small infrared target, one can obviously conclude that the following inequalities are satisfied:

$$T_C > G_N \Rightarrow T_C - G_N > 0 \quad (10a)$$

$$T_{N_1} > G_N \Rightarrow T_{N_1} - G_N > 0 \quad (10b)$$

$$T_{N_2} > G_N \Rightarrow T_{N_2} - G_N > 0 \quad (10c)$$

Eq. (10a)–(10c) are established only for one direction and similarly can be extended to the other three directions. Based on these equations, three convolution kernels can be constructed to distinguish between the target and non-target areas.

**Fig. 9** shows the constructed convolution kernels based on spatial distribution of the target model and the set of equations expressed in Eq. (10) which can be considered as an approximation to first order derivatives. The convolution kernels corresponding to these derivatives are depicted in **Fig. 9a–c**. Finally, by cumulating these kernel and considering the other three directions, the final convolution kernel is constructed (**Fig. 9d**). The result of applying this convolution kernel to an infrared image containing a small target close to high-intensity background clutter is shown in **Fig. 10c**. As shown in the figure, the proposed kernel effectively can enhance small targets close to the high-intensity background clutter.

The last drawback of the AAGD algorithm is related to high-intensity response to the sharp edges (**Fig. 5b**). This problem is not only limited to the AAGD algorithm, and almost all other detection algorithms also suffer from this limitation. The main reason that these algorithms are sensitive to sharp edges is because of two-dimensional filtering. While an image is a two-dimensional signal, performing a filtering process via two-dimensional kernel neglects directional information which is critical to distinguish between the target and non-target area in the field of small target detection. For example, a sharp edge only has large intensity variation in some directions while a small infrared target has relative contrast in all directions. based on this fact, a directional approach is presented to eliminate sharp edges and structural backgrounds and develop an effective small target detection algorithm. To this end, the proposed two-dimensional kernel which is based on cumulative derivatives (**Fig. 9d**) is broken into four different directions. These four directional cumulative derivative kernels are shown in **Fig. 11**.

After constructing cumulative directional derivative convolution kernels, the weighting coefficient for improved AAGD algorithm (Eq. (8)) is established using minimum response selection of cumulative directional derivatives. To this end, at each desired scale, every single kernel (**Fig. 11a–d**) is convolved with the original infrared image:

$$CDD_n = I * k_n \times H(I * k_n) \quad (11a)$$

$$CDD_e = I * k_e \times H(I * k_e) \quad (11b)$$

$$CDD_s = I * k_s \times H(I * k_s) \quad (11c)$$

$$CDD_w = I * k_w \times H(I * k_w) \quad (11d)$$

Then, the minimum response of the directional filtering results is considered as the output result to eliminate the high-intensity edges and structural backgrounds:

$$D_2 = \min\{CDD_n, CDD_e, CDD_s, CDD_w\} \quad (12)$$

Finally,  $D_2$  is used as a weighting coefficient for improved AAGD ( $D_1$ ):

**Table 1**  
Simulation parameters.

Parameter	Value	Comment
K	4	Number of scales
SE	$7 \times 7$	Size of structural element used in Tophat transform
$\Phi$	[ $3 \times 3, 5 \times 5, 7 \times 7, 9 \times 9$ ]	Size of AAGD's internal windows
$\Omega$	$19 \times 19$	Size of AAGD's external window
$\sigma$	[0.50, 0.60, 0.72, 0.86, 1.03, 1.24, 1.49, 1.79, 2.14, 2.57, 3.09, 3.71]	MS-LoG scale parameters [14]
P	[ $3 \times 3, 5 \times 5, 7 \times 7, 9 \times 9$ ]	Cell sizes in MS-PCM
LB	$25 \times 25$	Local background window for SCR calculation

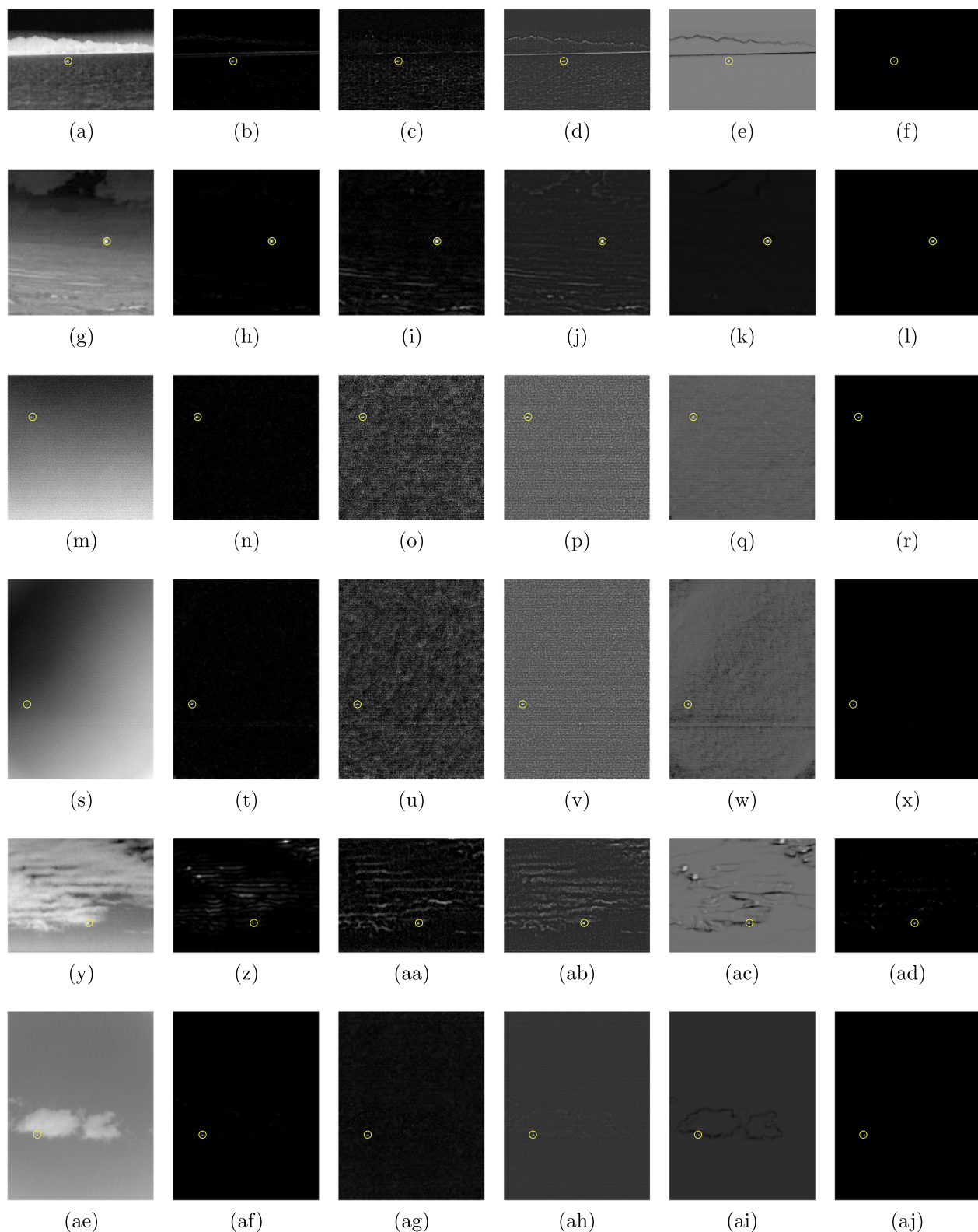


**Fig. 14.** Pre-thresholding results of the algorithms under the test on real infrared images (Target region is marked by yellow circle). From the left: **the first column:** original images, **the second column:** filtering results of MS-AAGD, **the third column:** filtering results of Tophat transform, **the fourth column:** filtering results of MS-LoG, **the fifth column:** filtering results of MS-PCM, **the sixth column:** filtering results of **the proposed method**.

**Table 2**

SCR values for the test targets.

Test image	MS-AAGD	Tophat transform	MS-LoG	MS-PCM	The proposed method
Fig. 14a	4.3729	1.9463	2.1338	3.7815	<b>52.1970</b>
Fig. 14g	17.3155	10.6199	13.9500	17.1423	<b>41.8991</b>
Fig. 14m	11.5877	3.1406	4.6522	8.0953	<b>33.2622</b>
Fig. 14s	10.8705	2.4651	3.4471	7.3387	<b>23.0154</b>
Fig. 14y	7.9095	6.5769	7.6839	3.0634	<b>26.1787</b>
Fig. 14ae	13.6938	5.2139	5.5948	6.2261	<b>36.7503</b>

**Table 3**

BSF values for the test images.

Test image	MS-AAGD	Tophat transform	MS-LoG	MS-PCM	The proposed method
Fig. 14a	11.1541	4.3257	4.8417	6.9720	<b>165.7378</b>
Fig. 14g	22.0500	4.5279	6.3295	24.8090	<b>82.0378</b>
Fig. 14m	14.0115	1.5496	2.8227	8.8367	<b>65.6961</b>
Fig. 14s	15.5447	1.7500	2.7646	5.7856	<b>82.6880</b>
Fig. 14y	2.6970	1.8764	2.4894	2.6615	<b>9.8939</b>
Fig. 14ae	28.4168	2.1795	3.0332	8.6323	<b>208.9080</b>

$$AAD_{CDD} = D_1 \times D_2 \quad (13)$$

Based on the stated information, using the cumulative directional derivative kernels addresses the second and the third limitations of the AAGD algorithm, simultaneously. Fig. 12 shows the edge removing feature of the proposed weighting coefficients.

The whole procedure of obtaining the weighting coefficients can be also performed in a multi-scale manner. In order to achieve multi-scale implementation, both improved AAGD ( $D_1$ ) and cumulative directional derivatives ( $D_2$ ) are calculated in different scales (3 × 3, 5 × 5, 7 × 7 and 9 × 9). In the final step, using a maximum selection along the scale dimension, the final result is achieved. Fig. 13 shows the overall procedure of the multi-scale implementation of the proposed algorithm.

#### Algorithm 1. The proposed algorithm

```

Input: Input Infrared Image  $I(x, y)$ , number of scales  $K$ 
Output: Filtered image  $Out(x, y)$ 
initialization: define  $\{\Phi^1, \Phi^2, \dots, \Phi^K\} < \Omega$  sets;
construct  $\{k_w^1, k_w^2, \dots, k_w^K\}$  kernels;
construct  $\{k_e^1, k_e^2, \dots, k_e^K\}$  kernels;
construct  $\{k_s^1, k_s^2, \dots, k_s^K\}$  kernels;
construct  $\{k_n^1, k_n^2, \dots, k_n^K\}$  kernels;
while  $(x, y) \in I(x, y)$  do
    for  $i = 1$  to  $K$  do
         $D_i^i(x, y) = |\mu_{\Phi^i} - \mu_{\Omega}|^2$ ;
        if  $\mu_{\Phi^i} < \mu_{\Omega}$  then
             $D_1^i(x, y) = 0$ ;
             $CDD_n^i(x, y) = I(x, y) * k_n^i(x, y)$ ;
             $CDD_e^i(x, y) = I(x, y) * k_e^i(x, y)$ ;
             $CDD_s^i(x, y) = I(x, y) * k_s^i(x, y)$ ;
             $CDD_w^i(x, y) = I(x, y) * k_w^i(x, y)$ ;
             $D_2^i(x, y) = \min \{CDD_n^i(x, y), CDD_e^i(x, y), CDD_s^i(x, y), CDD_w^i(x, y)\}$ ;
             $AAD_{CDD}^i(x, y) = D_1^i(x, y) \times D_2^i(x, y)$ ;
        Out(x, y) =  $\max\{AAD_{CDD}^1(x, y), AAD_{CDD}^2(x, y), \dots, AAD_{CDD}^K(x, y)\}$ 
    return Out(x, y)

```

#### 4. Simulation results

In order to investigate the performance of the proposed algorithm, simulation results on real infrared images containing small target are

provided in this section. To this end, the proposed algorithm as well as the multi-scale AAGD (MS-AAGD), the multi-scale LoG (MS-LoG), the multi-scale PCM (MS-PCM), and Tophat transform are implemented in MATLAB environment. Except for the MS-LoG which is constructed through 12 scales, the other multi-scale algorithms utilize four scales. Table 1 summarizes the simulation parameters which are used in this study. The test images contain a rich variety of false response sources like high-intensity edges (Fig. 14a, y, and ae), complicated background (Fig. 14g and y), noisy background (Fig. 14m and s), and a target maneuvering close to a high-intensity background clutter (Fig. 14y).

The detection ability of the proposed algorithm as well as the baseline algorithms is compared in both qualitative and quantitative manners. The visual enhancement of the filtered image is considered as qualitative performance. An ideal target detection algorithm is capable to map the whole input image (except target region) to zero value (black color) and only enhance the target region. As shown in Fig. 14, the proposed algorithm effectively rejects background clutter and enhances the target region.

In order to perform a quantitative comparison, two widely used metrics in the literature is chosen. The first one is signal to clutter ratio (SCR) which demonstrate target detection ability and is defined as follows:

$$SCR = \frac{f_T - f_b}{\sigma_b}, \quad (14)$$

where  $f_T$ ,  $f_b$ , and  $\sigma_b$  stand for the mean values of target pixels, the mean of the background region, and standard deviation of the local background, respectively.

Background suppression factor (BSF) shows the ability to eliminate background clutter and is expressed as:

$$BSF = \frac{\sigma_{in}}{\sigma_{out}}, \quad (15)$$

where  $\sigma_{in}$  and  $\sigma_{out}$  denote the standard deviation of the original input image and standard deviation of the filtered image, respectively.

The SCR and BSF values corresponding to the proposed algorithm as well as the baseline algorithms are reported in Tables 2 and 3, respectively. As reported in the tables, the proposed method significantly

outperforms the baseline algorithms.

While BSF and SCR are used to evaluate the detection algorithm before thresholding operation, false-alarm rate ( $P_{fa}$ ) is used to evaluate the clutter rejection ability of the small target detection algorithm after

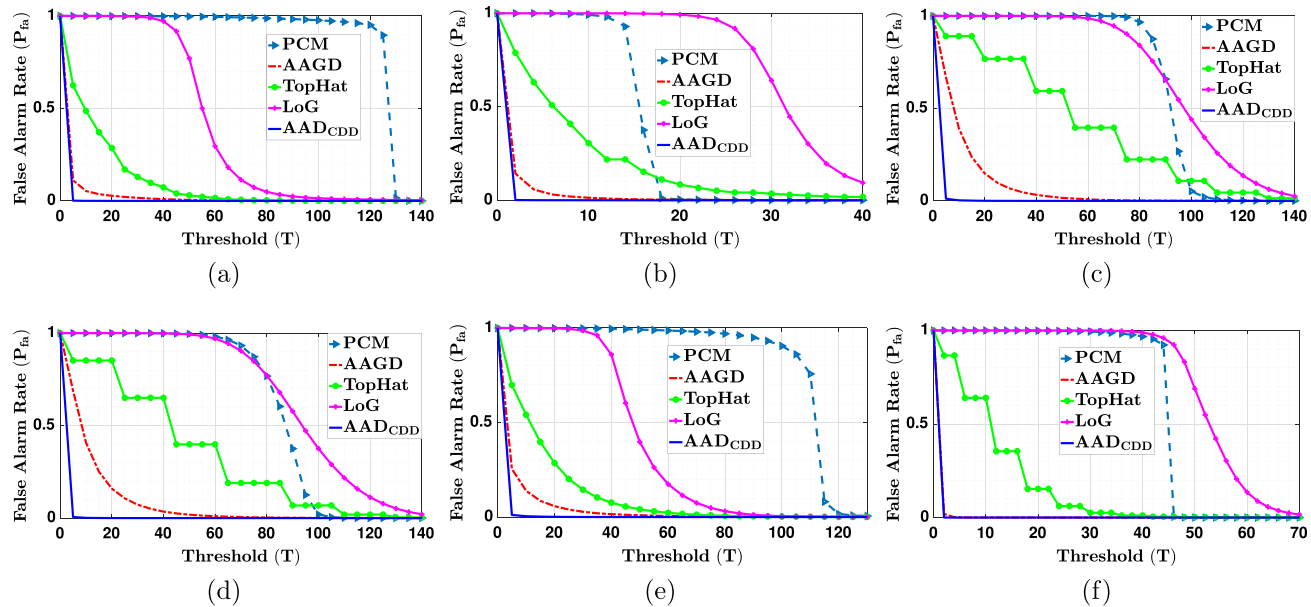


**Fig. 15.** False alarm rate versus threshold level curves for the different test images including: (a) Fig. 14a, (b) Fig. 14g, (c) Fig. 14m, (d) Fig. 14s, (e) Fig. 14y and (f) Fig. 14ae.

**Table 4**  
The full specifications of the implementation environment.

Operating System	Linux (Ubuntu 18.04, X64)
Linux kernel version	4.15.0-48-generic
OpenCV version	3.4.6
Compiler	GCC 7.4.0
Size of the test image	288 × 5600
Data depth and type	single channel 32 bit floating point
CPU	Intel CORE i7-8700 K @ 3.7 GHz
Memory	16 GB DDR4 @ 2400MT/s

**Table 5**  
The average execution time for the algorithms.

Detection method	Execution time (mS)
AAGD (4 scales)	171.041
LoG (12 scales)	317.745
PCM (4 scales)	2565.724
TopHat (single-scale with 7 × 7 SE)	3.893
the proposed method (4 scales)	259.349

thresholding process. The  $P_{fa}$  is defined as follows:

$$P_{fa} = \frac{N_f}{N_w} \quad (16)$$

where  $N_f$  and  $N_w$  are the total number of wrongly detected pixels and number of all pixels in the whole image, respectively [8]. Fig. 15 shows the  $P_{fa}$  versus global threshold level for the images under the test. As shown in the figure the proposed method has the lowest false responses compared to the other algorithm.

In order to demonstrate the computational complexity of each algorithm, All the algorithms are implemented using OpenCV C++ libraries.<sup>1</sup> The full specifications of the implementation environment are reported in Table 4. Each detection algorithm is executed 100 times and the average execution time for the algorithms are reported in Table 5.

<sup>1</sup> All the source codes are publicly available at <https://github.com/moradisaed>.

AS reported in the Table 5, the TopHat transform is the fastest algorithm due to its single-scale operation and relatively small structural element (SE). Among the multi-scale algorithms, AAGD has the lowest computational complexity. The proposed algorithm is slightly slower than AAGD algorithm because of utilizing extra convolution operators. While constructing single LoG operator takes less time than performing single-scale AAGD algorithm, the overall execution time for MS-LoG algorithm is almost double as compared to the AAGD algorithm. The MS-PCM has the highest computational complexity.

## 5. Conclusion

Infrared search and track (IRST) systems have attracted more attention in recent years due to advances of infrared imaging technology and having special characteristics like covert operation and resistance against jamming. However, detecting long-distant targets in these systems is a challenging and difficult task. Despite the progress of the small infrared target detection algorithms in recent years, there are still two unsolved challenges related to small target detection: (1) intensifying high-intensity structural backgrounds, and (2) missing targets which are maneuvering close to a high-intensity background clutter. In this paper, in the first step, the major drawbacks of one of the most effective target detection algorithms called average absolute gray difference (AAGD) are investigated precisely. Then, in a three step procedure, the deficiencies of the AAGD algorithms are eliminated using proper weighting coefficients which are derived from the proposed cumulative directional derivatives. Simulation results on real infrared images which contain a rich variety of false response sources like high-intensity edges, complicate background, noisy background, and a target maneuvering close to a high-intensity background clutter prove the significant effectiveness of the proposed algorithm.

## Declaration of Competing Interest

The authors declare that there are no conflicts of interest regarding the publication of this paper.

## References

- [1] X. Bai, Y. Bi, Derivative entropy-based contrast measure for infrared small-target detection, IEEE Trans. Geosci. Remote Sens. 56 (4) (2018) 2452–2466.

- [2] Y. hong Xin, J. Zhou, Y. shuan Chen, Dual multi-scale filter with SSS and GW for infrared small target detection, *Infrared Phys. Technol.* 81 (12) (2017) 97–108.
- [3] D. Liu, L. Cao, Z. Li, T. Liu, P. Che, Infrared small target detection based on flux density and direction diversity in gradient vector field, *IEEE J. Sel. Top. Appl. Earth Observ. Remote Sens.* (99) (2018) 1–27.
- [4] L. Deng, J. Zhang, H. Zhu, Infrared moving point target detection using a spatial-temporal filter, *Infrared Phys. Technol.* 95 (10) (2018) 122–127.
- [5] P. Khaledian, S. Moradi, E. Khaledian, A new method for detecting variable-size infrared targets, *Sixth International Conference on Digital Image Processing, International Society for Optics and Photonics, 2014*pp. 91591J–91591J.
- [6] X. Zhang, Q. Ding, H. Luo, B. Hui, Z. Chang, J. Zhang, Infrared small target detection based on directional zero-crossing measure, *Infrared Phys. Technol.* 87 (2017) 113–123.
- [7] S. Moradi, P. Moallem, M.F. Sabahi, A false-alarm aware methodology to develop robust and efficient multi-scale infrared small target detection algorithm, *Infrared Phys. Technol.* 89 (2018) 387–397.
- [8] S. Moradi, P. Moallem, M.F. Sabahi, Scale-space point spread function based framework to boost infrared target detection algorithms, *Infrared Phys. Technol.* 77 (2016) 27–34.
- [9] S.D. Deshpande, M.H. Er, R. Venkateswarlu, P. Chan, Max-mean and max-median filters for detection of small targets, *Signal and Data Processing of Small Targets 1999, vol. 3809, International Society for Optics and Photonics, 1999*, pp. 74–84.
- [10] M. Zeng, J. Li, Z. Peng, The design of top-hat morphological filter and application to infrared target detection, *Infrared Phys. Technol.* 48 (1) (2006) 67–76.
- [11] X. Wang, Z. Peng, D. Kong, P. Zhang, Y. He, Infrared dim target detection based on total variation regularization and principal component pursuit, *Image Vis. Comput.* 63 (2017) 1–9.
- [12] S. Kim, Double layered-background removal filter for detecting small infrared targets in heterogenous backgrounds, *J. Infrared Millimeter Terahertz Waves* 32 (1) (2011) 79–101.
- [13] S. Kim, Y. Yang, J. Lee, Y. Park, Small target detection utilizing robust methods of the human visual system for irst, *J. Infrared Millimeter Terahertz Waves* 30 (9) (2009) 994–1011.
- [14] S. Kim, J. Lee, Scale invariant small target detection by optimizing signal-to-clutter ratio in heterogeneous background for infrared search and track, *Pattern Recogn.* 45 (1) (2012) 393–406.
- [15] C.P. Chen, H. Li, Y. Wei, T. Xia, Y.Y. Tang, A local contrast method for small infrared target detection, *IEEE Trans. Geosci. Remote Sens.* 52 (1) (2014) 574–581.
- [16] J. Han, K. Liang, B. Zhou, X. Zhu, J. Zhao, L. Zhao, Infrared small target detection utilizing the multiscale relative local contrast measure, *IEEE Geosci. Remote Sens. Lett.* 15 (4) (2018) 612–616.
- [17] Y. Qin, B. Li, Effective infrared small target detection utilizing a novel local contrast method, *IEEE Geosci. Remote Sens. Lett.* 13 (12) (2016) 1890–1894.
- [18] H. Deng, X. Sun, M. Liu, C. Ye, X. Zhou, Infrared small-target detection using multiscale gray difference weighted image entropy, *IEEE Trans. Aerosp. Electron. Syst.* 52 (1) (2016) 60–72.
- [19] Y. Wei, X. You, H. Li, Multiscale patch-based contrast measure for small infrared target detection, *Pattern Recogn.* 58 (2016) 216–226.
- [20] R.N. Strickland, H.I. Hahn, Wavelet transform methods for object detection and recovery, *IEEE Trans. Image Process.* 6 (5) (1997) 724–735.